

Intercode comparison of gyrokinetic global electromagnetic modes

T. Görler, N. Tronko, W. A. Hornsby, A. Bottino, R. Kleiber, C. Norscini, V. Grandgirard, F. Jenko, and E. Sonnendrücker

Citation: *Physics of Plasmas* **23**, 072503 (2016); doi: 10.1063/1.4954915

View online: <http://dx.doi.org/10.1063/1.4954915>

View Table of Contents: <http://scitation.aip.org/content/aip/journal/pop/23/7?ver=pdfcov>

Published by the [AIP Publishing](#)

Articles you may be interested in

[Quantitative comparison of electron temperature fluctuations to nonlinear gyrokinetic simulations in C-Mod Ohmic L-mode discharges](#)

Phys. Plasmas **23**, 042303 (2016); 10.1063/1.4945620

[Quasilinear saturation of the aperiodic ordinary mode streaming instability](#)

Phys. Plasmas **22**, 092301 (2015); 10.1063/1.4929852

[Applications of large eddy simulation methods to gyrokinetic turbulence](#)

Phys. Plasmas **21**, 032304 (2014); 10.1063/1.4868235

[Linear and nonlinear verification of gyrokinetic microstability codes](#)

Phys. Plasmas **18**, 122505 (2011); 10.1063/1.3671907

[Fluctuations and discrete particle noise in gyrokinetic simulation of drift waves](#)

Phys. Plasmas **14**, 032307 (2007); 10.1063/1.2710808



PFEIFFER VACUUM

VACUUM SOLUTIONS FROM A SINGLE SOURCE

Pfeiffer Vacuum stands for innovative and custom vacuum solutions worldwide, technological perfection, competent advice and reliable service.

Intercode comparison of gyrokinetic global electromagnetic modes

T. Görler,^{1,a)} N. Tronko,¹ W. A. Hornsby,¹ A. Bottino,¹ R. Kleiber,² C. Norscini,³
 V. Grandgirard,³ F. Jenko,⁴ and E. Sonnendrücker¹

¹Max Planck Institute for Plasma Physics, Boltzmannstr. 2, 85748 Garching, Germany

²Max Planck Institute for Plasma Physics, Wendelsteinstr. 1, 17491 Greifswald, Germany

³CEA, IRFM, F-13108 Saint-Paul-lez-Durance, France

⁴Department of Physics and Astronomy, University of California, Los Angeles, California 90095, USA

(Received 25 March 2016; accepted 31 May 2016; published online 5 July 2016)

Aiming to fill a corresponding lack of sophisticated test cases for global electromagnetic gyrokinetic codes, a new hierarchical benchmark is proposed. Starting from established test sets with adiabatic electrons, fully gyrokinetic electrons, and electrostatic fluctuations are taken into account before finally studying the global electromagnetic micro-instabilities. Results from up to five codes involving representatives from different numerical approaches as particle-in-cell methods, Eulerian and Semi-Lagrangian are shown. By means of spectrally resolved growth rates and frequencies and mode structure comparisons, agreement can be confirmed on ion-gyro-radius scales, thus providing confidence in the correct implementation of the underlying equations.

[<http://dx.doi.org/10.1063/1.4954915>]

I. INTRODUCTION

Over the past two decades, gyrokinetic^{1,2} codes have experienced an amazing development of their abilities and comprehensiveness regarding relevant physics effects.³ A major step along these lines is the self-consistent treatment of electromagnetic fluctuations with fully gyrokinetic electrons. Fluxtube (local) domain implementations have repeatedly and extensively been benchmarked against each other in this context—see, e.g., Refs. 4–7. However, apart from a few examples in extremely simplified setups, e.g., Ref. 8 with flat temperature profiles, similar efforts can rarely be found between the various radially global gyrokinetic codes. This may very well be linked to the increased complexity and the computational expenses associated to this task. Since alternative comparisons with (semi-) analytical results are naturally just feasible in very restricted physical parameter sets, inter-code benchmark studies can be considered as an important step towards verification. A new test case is hence defined and results from a number of codes with very different numerical approaches are presented in the following. The structure is as follows: The chosen physical scenario and the employed numerical tools are briefly discussed in Sec. II. Hereafter, the benchmark parameters are detailed in Sec. III before the actual results are discussed in Sec. IV. A summary and idea for further extensions of this exercise to turbulent regimes are given in Sec. V.

II. PHYSICAL SCENARIO AND NUMERICAL TOOLS

The idea is to build upon preceding successful benchmark studies which were performed without electromagnetic fluctuations, i.e., by neglecting Ampère's law and the electromagnetic fields in the coupled gyrokinetic Vlasov-Maxwell system of equations. These cases shall be extended accordingly in order to reduce the effort regarding the definition and comparison of secondary parameters which are required

for the test case itself but rather irrelevant for the general inclusion of electromagnetic fluctuations, for instance, the profiles and the geometry. Among others, the ITM 2008 benchmark,⁹ the GYRO/GTC¹⁰ comparison, and similar GENE/ORB5 benchmarks^{11,12} can be identified as possible starting point as they all present comparisons of completely different numerical approaches, e.g., Eulerian vs. Lagrangian methods. All of the listed examples are inspired and are based on the Cyclone Base Case^{13,14} (CBC) which is a well established reference scenario in flux tube studies. However, the individual benchmarks differ in details like assumptions regarding the specific shape of the temperature, density, and safety factor profiles, and the basic setups which consider decaying or gradient-driven turbulence or linear mode characterization. Due to the significantly higher complexity linked to a fully gyrokinetic treatment of electrons and the consideration of electromagnetic fluctuations, the proposed test case will be restricted to linear physics for now and shall be extended to a nonlinear benchmark in a next step. Therefore, Ref. 12, Sec. III appears to offer an adequate basis where the dominant toroidal modes (maximized over all poloidal (m) modes) are compared. The parameters and the extension from the original adiabatic electron benchmark to an electromagnetic test case will be detailed in Section III. The numerical tools employed at the various stages of this code-comparison involve up to five independently developed codes based on three entirely different approaches—namely, Eulerian, Lagrangian, and semi-Lagrangian methods. The first scheme sometimes also referred to as “Vlasov” solves the gyrokinetic Vlasov-Maxwell system of equations on a fixed grid in phase space. It is considered in the two δf -codes GENE^{15,16} and GKW^{17,18} that are contributing to this benchmark. Here, δf indicates that the distribution function is split into a background and a fluctuating part where only the latter has to be propagated in time. This splitting is also employed in the Lagrangian codes ORB5^{19–21} and EUTERPE²² where the gyrokinetic equations are solved with “particle-in-cell” (PIC) methods. The latter involve sampling the initial positions in

^{a)}Electronic mail: tobias.goerler@ipp.mpg.de

phase space, following marker orbits in 5D and obtaining the source terms for the field equations at every timestep. Finally, results from the full- f code GYSELA^{23,24} are shown. Here, a fixed phase space grid is employed like in Eulerian codes. However, the Vlasov equation is evaluated by integration along the trajectories utilizing the associated invariance of the distribution function. The new values of the distribution function on the grid are finally evaluated with interpolation methods. Further details regarding these schemes and implementations can be obtained from the above mentioned code references or, e.g., from Refs. 2 and 3.

III. PARAMETERS RELEVANT TO THE BENCHMARK

An overview of the parameters for the code comparison is presented in the following. As mentioned before, the test case is based on the linear benchmark in Ref. 12 which in turn is inspired by the CBC parameters.¹³

Though the original discharge¹⁴ serving as basis for the CBC had naturally more complex shaped flux surfaces, a circular concentric magnetic equilibrium (see, e.g., Ref. 25 and Appendix A) with inverse aspect ratio $a/R_0 = 0.36$ and safety factor profile,

$$q(r) = 2.52(r/a)^2 - 0.16(r/a) + 0.86, \quad (1)$$

see Fig. 1, is taken here for simplicity. Here, a and R_0 denote the minor and major tokamak radii while r is the local radius of a flux surface. Consistently with the choice of concentric surfaces, Shafranov shifts are absent and by considering the pressure gradient (∇p) contribution to the curvature or ∇B -drift as a magnetic equilibrium effect ($\nabla p \sim \beta' \sim \alpha_{\text{MHD}} = 0$), it is *neglected* in the following as well. More complicated test cases where the magnetic equilibrium and the equilibrium pressure gradient are evaluated self-consistently (e.g., a generalized, global *Miller equilibrium*²⁶) are left for future work—the focus here is to study the effect of the additional electromagnetic fields only.

The temperature and density profiles and their normalized logarithmic gradients are given by

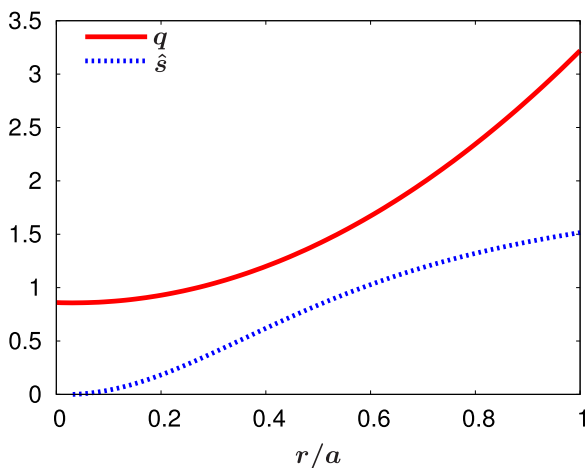


FIG. 1. Radial safety factor q (solid line) and magnetic shear $\hat{s} = r/q dq/dr$ (dashed line) profile.

TABLE I. List of parameters relevant to the benchmark.

r_0/a	0.5
a/L_{ref}	0.36
R_0/L_{ref}	1.0
$T_i(r_0)/T_{\text{ref}} = T_e(r_0)/T_{\text{ref}}$	1.0
$\kappa_{T_i} = \kappa_{T_e}$	6.96
$w_{T_i} = w_{T_e}$	0.3
$n_i(r_0)/n_{\text{ref}} = n_e(r_0)/n_{\text{ref}}$	1.0
$\kappa_{n_i} = \kappa_{n_e}$	2.23
$w_{n_i} = w_{n_e}$	0.3
m_i/m_{ref}	1.0
m_e/m_{ref}	5.44617×10^{-4}

$$A/A(r_0) = \exp \left[-\kappa_A w_A \frac{a}{L_{\text{ref}}} \tanh \left(\frac{r-r_0}{w_A a} \right) \right], \quad (2)$$

$$L_{\text{ref}}/L_A = -L_{\text{ref}} \partial_r \ln A(r) = \kappa_A \cosh^{-2} \left(\frac{r-r_0}{w_A a} \right), \quad (3)$$

which represent a peaked gradient profile of $A = (n, T)$ with characteristic width w_A , maximum amplitude κ_A , and center at r_0 . Furthermore, L_{ref} denotes the macroscopic reference length that will be fixed to the major radius R_0 in the following. The individual values of the quantities are summarized in Table I which reveals that the temperature and density profiles are chosen to be identical for ions and electrons. A visual impression of the profiles can be found in Fig. 2.

The nominal reference values which are again inspired by Ref. 14, Fig. 5 at $\rho = 0.5$ (assuming that this corresponds to $r/a = 0.5$ if reshaped into the circular concentric equilibrium at hand), are listed in Table II. Here, only one ion species—namely, deuterium—is considered consistently with the main ion species in the underlying experimental setup. The associated finite-size parameter ρ^* , here defined as the ion-gyroradius-to-minor-radius ratio, is hence approximately 1/180. Nevertheless, the ion-to-electron mass ratio is set to the proton-electron mass ratio—i.e., the electrons are two times heavier than in reality—in order to reduce the resolution requirements and the computational effort. Considering hydrogen ions, on the other hand, would further decrease the value of ρ^* and would hence yield less significant finite-size effects which appear not to be desirable for a global code benchmark. Additionally, a correct ρ^* for the ions might be more striking in the spectral range under consideration than a correct $\rho_e^* = \rho_e/a$ for the electron species. Finally, we note that the nominal β value at $r/a = 0.5$ is very close to 1% if the definition $\beta_{\text{ref}} = 8\pi n_{\text{ref}} T_{\text{ref}} / B_{\text{ref}}^2$ is employed. Here, n_{ref} and T_{ref} denote reference density and temperature taken at $r/a = 0.5$ and B_{ref} is the toroidal magnetic field on axis. As the definition of β may be different in the various codes, scans over β will also be represented by accordingly varying reference densities n_{ref} . Since collision frequency ν_{coll} and Debye wavelength λ_{Debye} are assumed to be zero for simplicity, changes in n_{ref} should indeed have no further impact other than those caused by the kinetic-to-magnetic-pressure ratio.

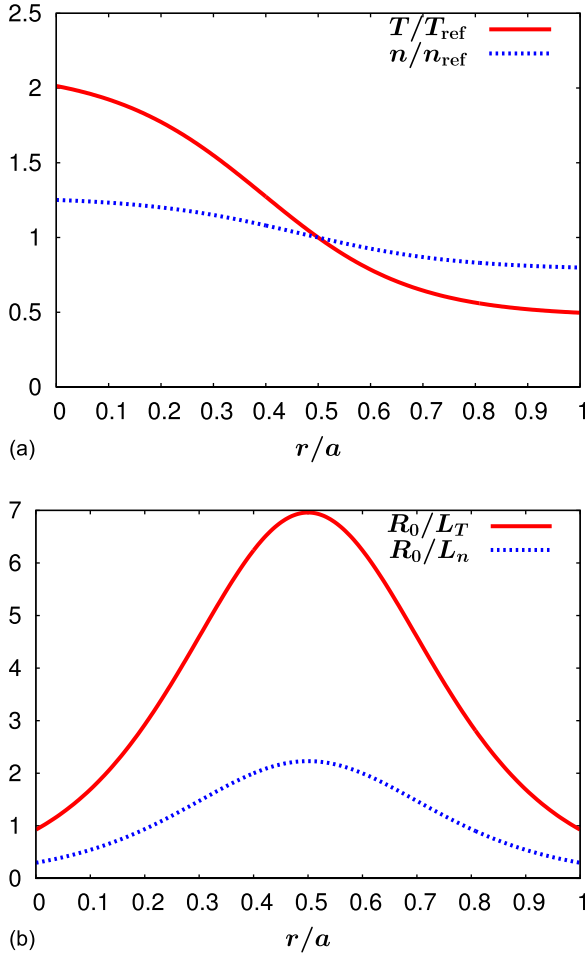


FIG. 2. Radial (a) temperature (solid line) and density (dashed line) and (b) their normalized logarithmic gradient profiles as defined in Eq. (3) and Tables I and II.

IV. NUMERICAL RESULTS AND COMPARISONS

This section contains the actual benchmark results. While the ultimate goal of this paper is the comparison of linear (toroidal) modes with self-consistent treatment of \tilde{A}_{\parallel} fluctuations (parallel magnetic fluctuations \tilde{B}_{\parallel} are neglected for now and hardly available in any of the participating global codes), the intermediate steps, i.e., (A) the original adiabatic electron case and (B) the extension to gyrokinetic electrons but electrostatic fluctuations are presented as well. This way, we hope to improve the accessibility and

TABLE II. Nominal reference and derived reference values inspired by the low elongation case (CBC) in Ref. 14, Fig. 5 at $\rho = 0.5$.

$m_{\text{ref}} (= m_D)/m_p$	2.0
$n_{\text{ref}} (= n_e)/10^{19} \text{m}^{-3}$	4.66
$T_{\text{ref}} (= T_e^{\text{exp}})/\text{keV}$	2.14
$B_{\text{ref}} (= B_t(R_{\text{mag}}))/\text{T}$	2.0
$L_{\text{ref}} (= R_0 = R_{\text{mag}})/\text{m}$	1.67
β_{ref}	0.0101
$\rho^* = \rho_s/a$	$0.00555 \sim 1/180.2$
ν_{coll}	0
λ_{Debye}	0

reproducibility of this benchmark for other codes. For the sake of a quick comparison, tabulated results are added for each of the steps for at least one of the participating codes while the benchmark results will be shown in dedicated plots.

A. Ion temperature gradient (ITG) mode with adiabatic electron response

First of all, the one-species simulation results in Ref. 12, Fig. 2, are reproduced and can be found in Fig. 3 and Table III. More specifically, the spectral properties of linear growth rates and real frequencies are displayed and describe a pure ion temperature gradient (ITG) driven mode since positive frequencies indicate modes drifting in the ion diamagnetic drift direction. For convenience, two abscissa are included where the lower one is the integer valued toroidal mode number n_0 which serves as a rather code independent measure while the upper one is the binormal wave number $k_y = n_0 q(r_0)/r_0$ at the center of the simulation domain. The latter is normalized to $\rho_s = c_s/\Omega$ with ion sound speed $c_s = \sqrt{T_{\text{ref}}/m_{\text{ref}}}$ and cyclotron frequency $\Omega = eB_{\text{ref}}/(m_{\text{ref}}c)$. The growth rates and frequencies are given in normalized units c_s/R_0 as well as SI units. The hardly visible error bars mark statistical uncertainties based on the time evolution of these quantities, e.g., in the cases where they are still oscillating. Systematic errors, e.g., linked to numerical resolution, are not taken into account—all codes were asked to provide sufficiently numerically converged results. GENE flux-tube results maximized over the radial domain are shown as well since they provide a cheap consistency check. As a result of the effectively reduced linear

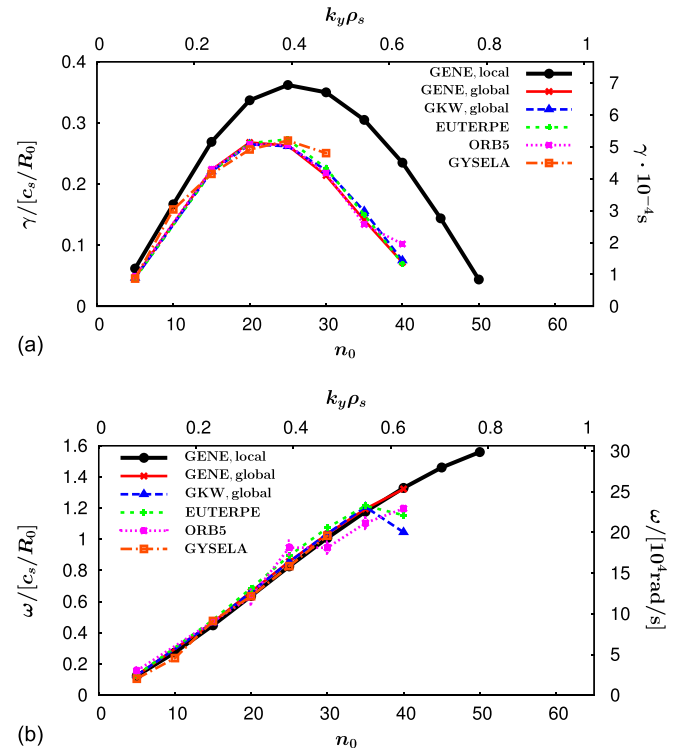


FIG. 3. Linear (a) growth rate and (b) real frequency spectra for the one-species, adiabatic electrons case from EUTERPE, GENE, GKW, GYSELA, and ORB5. The local (flux tube) are plotted for reference, as well.

TABLE III. Data points from global GENE simulations as presented in Fig. 3 for the adiabatic electron case. Growth rates and frequencies (γ, ω) are normalized to $c_s/R_0 = 191.7$ kHz.

n_0	$k_y \rho_s$	γ_{GENE}	ω_{GENE}
5	0.078	0.048	0.127
15	0.235	0.223	0.467
20	0.313	0.268	0.664
25	0.391	0.263	0.857
30	0.470	0.214	1.034
35	0.548	0.141	1.195
40	0.626	0.072	1.322

drive, the global code results should always exhibit lower growth rate amplitudes while—in the absence of mode transitions—good agreement is typically found in the real frequencies. These features are well reproduced by all global codes, namely, EUTERPE, GENE, GKW, GYSELA, and ORB5, in Fig. 3. Furthermore, all the codes agree very well at low wave numbers—despite their rather different numerical approaches, see Sec. II. Some deviations can, however, be observed at higher wave numbers ($n_0 \geq 35$). The reasons are two-fold. Some of the codes are not able to separate and deactivate the non-linear terms. The statistical analysis is hence restricted to the initial linear phase of the simulation which may be too short for a reliable value. This is why, for instance, no GYSELA data is available beyond $n_0 = 35$. Furthermore, only GENE and GKW have been run with high- k suitable gyro-average operators, all other participating codes have here been using low- k approximations like truncated Taylor or Padé expansions such that differences around $k_y \rho_s \sim 0.5$ can be expected. Finally, the frequency mismatches even between GENE and GKW at $n_0 = 40$ can be related to the very low growth rate and the existence of strong sub-dominant modes which complicate the identification of the dominant ones. However, overall, the agreement in growth rate and frequency can be considered remarkable. Of course, additional features can be compared as well. For instance, poloidal cross sections of the $n_0 = 25$ mode of the electrostatic potential ϕ from the Eulerian code GENE and the PIC code ORB5 are shown in Fig. 4. Both codes

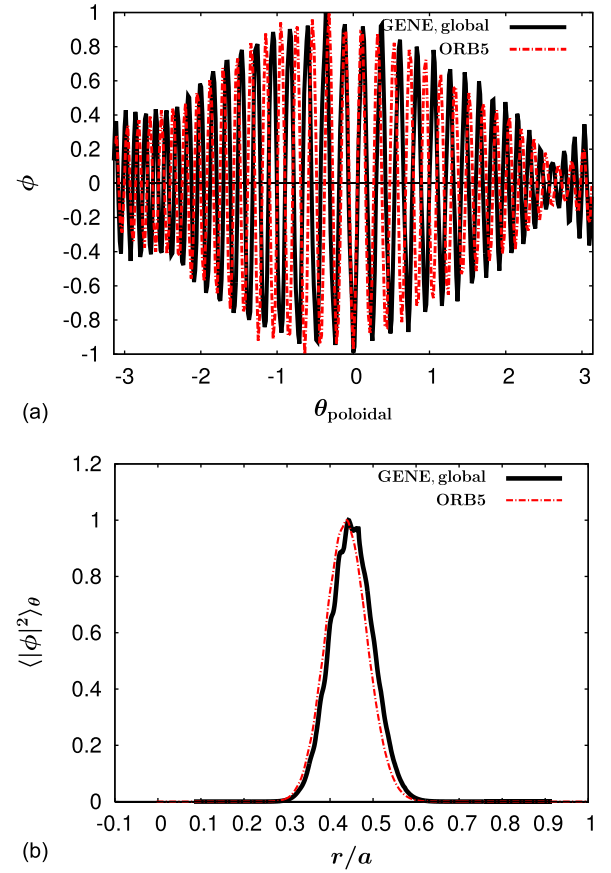


FIG. 5. Direct comparison of the last snapshot of the electrostatic potential at $n = 25$ from GENE and ORB5 (a) as function of the poloidal angle at $r/a = 0.5$ (phase adjusted to the dominant poloidal mode number m) and (b) as radial profile of the poloidally averaged squared fluctuations.

exhibit very similar eddy structures that are only weakly tilted and peaked around the maximum logarithmic gradient. For a more detailed comparison, poloidal and radial profiles have been evaluated as well. The simulation results have first been mapped from the straight-field-line to the poloidal angle at $r/a = 0.5$ and then adjusted to the dominant poloidal m mode (30 in ORB5 and 27 in GENE) for the former which is presented in Fig. 5(a). The radial profiles shown in Fig. 5(b) are derived

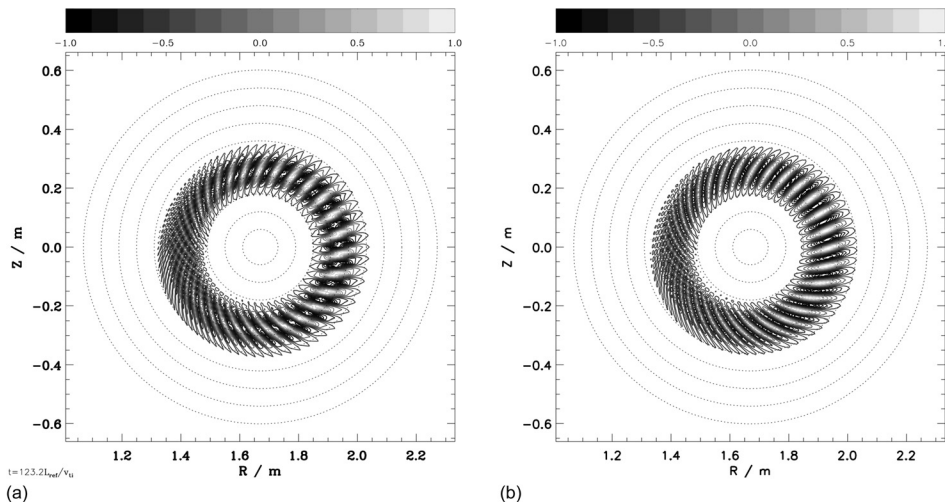


FIG. 4. Mode structure of the rescaled electrostatic potential in the (R, Z) plane from (a) GENE and (b) ORB5 for the one species (adiabatic electrons) case for $n_0 = 25$.

by simply summing the squared fluctuations of ϕ over the poloidal angle and renormalizing to the maximum of the radial envelope. Good agreement can be observed in both profiles although a slight shift in the radial envelope and a difference at the inboard side ($\theta_{\text{poloidal}} = \pm\pi$) in the poloidal structure can be seen.

B. Two-species electrostatic simulations

In an intermediate step towards studies of electromagnetic microinstabilities, the electron response is now switched from adiabatic to fully gyrokinetic while still only electrostatic fluctuations are considered. Nevertheless, the linear findings are already altered substantially. As can be seen in Fig. 6 and Table IV, the low- k spectrum is still dominated by an ITG mode, however, with almost twice as large growth rate. Furthermore, a transition to modes propagating in electron diamagnetic drift direction ($\omega < 0$) can now be observed around $n_0 = 40$ and 50 therefore indicating additional trapped electron modes (TEMs) or TEM/ETG-hybrid modes. The codes participating in this step—GENE, GKW, and ORB5—demonstrate good agreement at low- k . Above $n_0 = 40$, ORB5 finds significantly lower growth rates and misses the mode transition. This is, however, well understood and linked to the low- k truncation in the field solver²⁷ while the two Eulerian codes employ higher or arbitrary order schemes.¹⁶ A more comprehensive solver is currently under development in ORB5 and first results will be published soon.²⁸

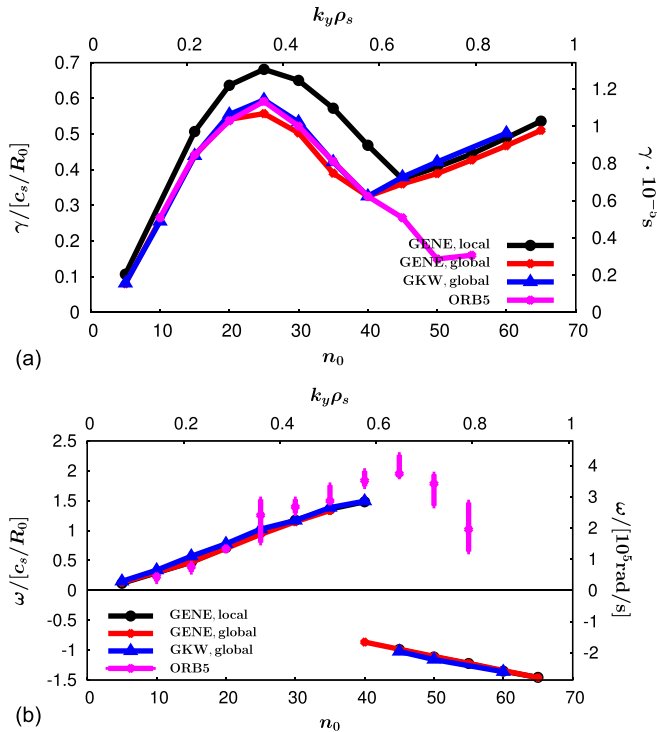


FIG. 6. Linear (a) growth rate and (b) real frequency spectra from GENE, ORB5, and GENE for the electrostatic case. The local (flux tube) results with linear growth rates maximized over the radius and ballooning angle are plotted for reference, as well.

TABLE IV. Data points from global GENE simulations as presented in Fig. 6 for the electrostatic case. Growth rates and frequencies (γ, ω) are normalized to $c_s/R_0 = 191.7$ kHz.

n_0	$k_y \rho_s$	γ_{GENE}	ω_{GENE}
5	0.078	0.080	0.132
15	0.235	0.439	0.472
20	0.313	0.541	0.702
25	0.391	0.557	0.936
30	0.470	0.503	1.147
35	0.548	0.390	1.335
40	0.626	0.325	-0.865
45	0.704	0.360	-0.984
50	0.783	0.389	-1.103
55	0.861	0.427	-1.221
60	0.939	0.467	-1.340
65	1.017	0.510	-1.461

Again, local (flux-tube) growth rates are additionally shown in Fig. 6 which are maximized over radius and ballooning angle. Like before, the local and global frequencies are found to be in good agreement—except for the dominant mode transition marked by a jump in frequency which appears to be shifted to a slightly lower wave number. This is in line with a substantial reduction of the ITG growth rate (as in the adiabatic electron case) and the marginal decrease of the TEM/ETG growth rate (comparing the results from the two GENE versions—GKW seems to show systematically slightly larger growth rates). The small difference in the high- k branch may be attributed to the dominance of the electron physics for these modes. With ρ_e^* being about a factor of 60 smaller, finite-size effects would indeed be less significant or even negligible.

The mode structures of the electrostatic potential at $n_0 = 25$ from representatives of the Eulerian and PIC codes are shown in Figs. 7 and 8. The agreement can be considered satisfying. The main difference is found at mode rational surfaces where electrons cannot become adiabatic. While GENE exhibits circular structures in the 2D contours or, respectively, spikes in the radial profiles at such surfaces, such structures are hardly visible in the ORB5 results. It is highly unlikely that this finding is linked to ORB5 being actually run with the full electromagnetic version at $\beta = 10^{-4}$ for technical reasons. This setup should well agree with the electrostatic limit. However, the differences can again be related to the here employed low- k approximation²⁷ in the ORB5 gyro-average operator which introduces a smoothing of such fine-scale structures. Corresponding details will be discussed in Ref. 28. Here, it shall be noted that the effect on the growth rate at $n_0 = 25$ is apparently only minor. However, as has been found by both GKW and GENE, properly resolving such structures seems at least to be crucial at higher wave numbers ($n_0 \geq 35$) and at the lowest toroidal mode. At these scales, the widths of the mode rational surfaces become particularly small and at high n_0 the surfaces themselves are much more frequent as can be seen in Fig. 7(c). The required radial resolution is hence $\leq 0.08\rho_s$ which is almost one order of magnitude less than in the adiabatic electron case.

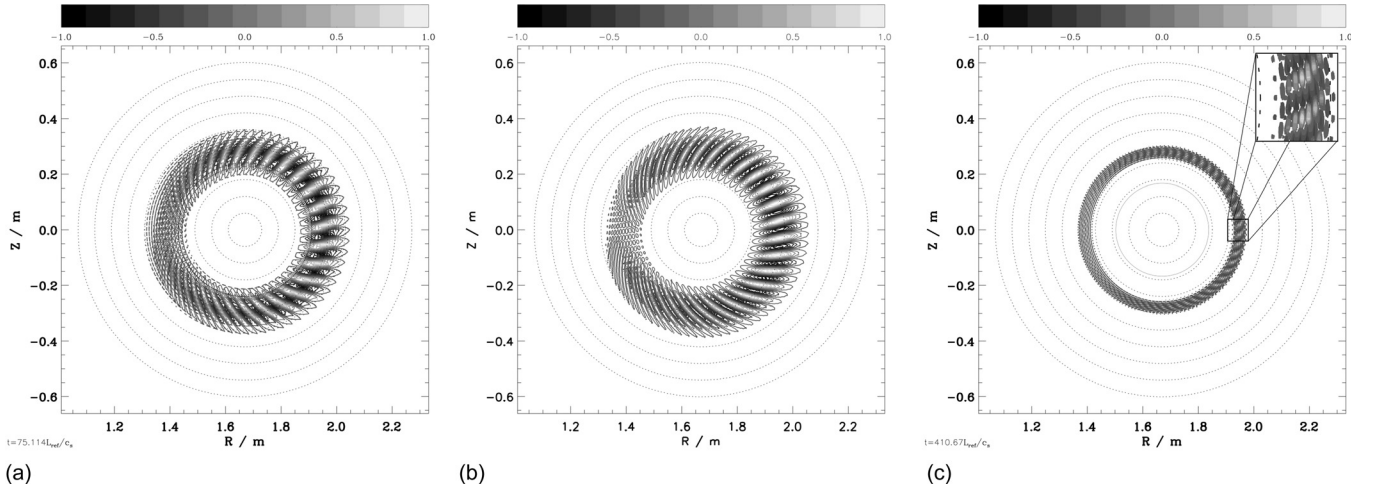


FIG. 7. Mode structure of the rescaled electrostatic potential in the (R,Z) plane for the electrostatic 2 species case at $n_0 = 25$ (a) from GENE and (b) from ORB5, and (c) at $n_0 = 50$ from GENE including a zoom into the cross section at the low field side.

C. Electromagnetic two-species studies

After these preparatory comparisons, the actual target can be addressed and electromagnetic test cases are defined and presented in this subsection. On the one hand, they contain a parametric study of the influence of electromagnetic fluctuations controlled by β_{ref} or n_{ref} , respectively, on a linear mode at fixed $n_0 = 19$ ($k_y \rho_s = 0.3$). Furthermore, spectral properties at the nominal β value as defined in Table II are studied.

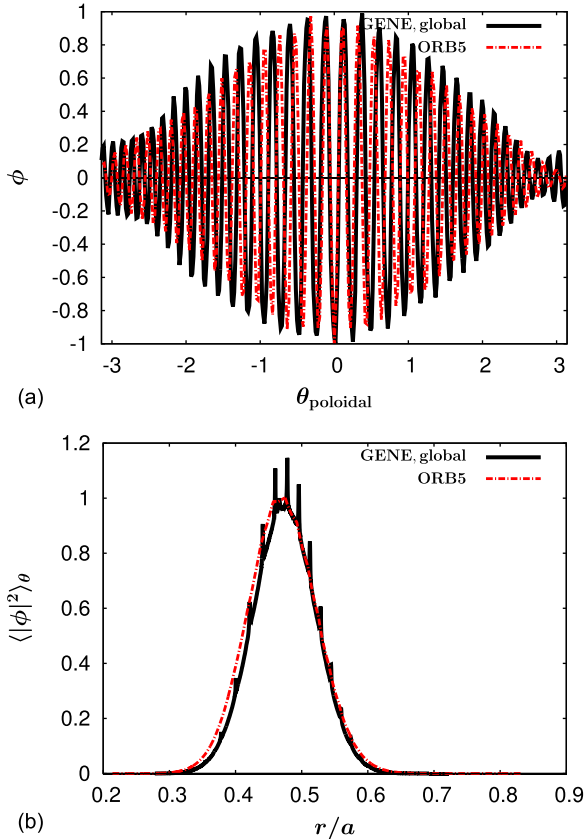


FIG. 8. Direct comparison of the last snapshot of the electrostatic potential at $n = 25$ from GENE and ORB5 (a) as function of the poloidal angle at $r/a = 0.5$ (phase adjusted to the dominant poloidal mode number m) and (b) as radial profile of the poloidally averaged squared fluctuations.

1. Variation of β at fixed wave number

Keeping the toroidal mode number fixed at $n_0 = 19$ which translates to $k_y \rho_s \approx 0.3$, a scan over the reference density and hence over β is performed. As can be observed in Fig. 9 and Table V, the ITG mode is stabilized with increasing β , for instance, by more than 25% at the nominal value compared to the electrostatic ($\beta = 0$) case, hence emphasizing the need for electromagnetic simulations in particular, experimental scenarios like the CBC.

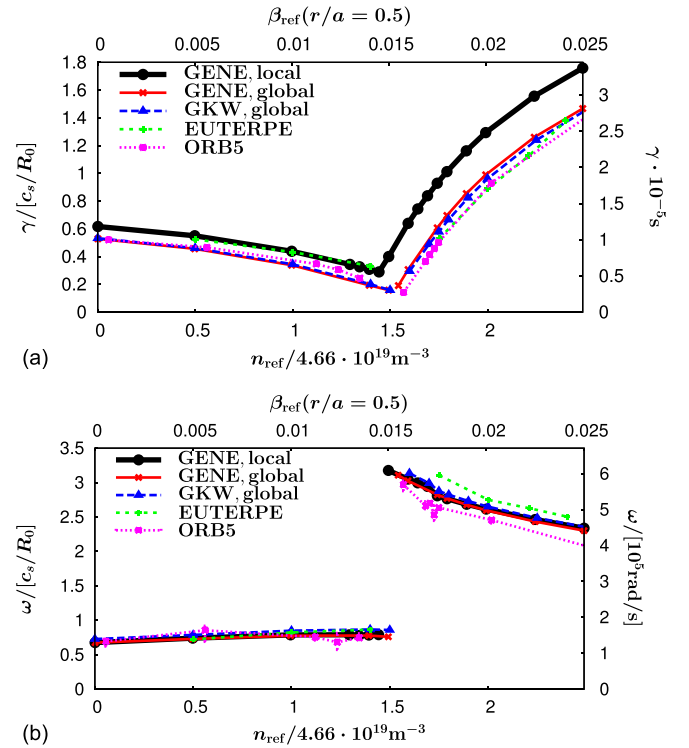


FIG. 9. Linear (a) growth rates and (b) real frequencies from GENE, GWK, ORB5, and EUTERPE as function of β (upper abscissa) or the reference density (lower abscissa), respectively, at fixed toroidal wave number $n_0 = 19$. The local (flux tube) GENE results with linear growth rates maximized over the radius and ballooning angle are plotted for reference, as well.

TABLE V. Data points from global GENE simulations as presented in Fig. 9 for the β scan at $n_0 = 19$ ($k_y \rho_s \sim 0.3$). The growth rates and frequencies are given in $c_s/R_0 = 191.7$ kHz.

$n_{\text{ref}}/4.66 \times 10^{19} \text{ m}^{-3}$ $\approx \beta_{\text{ref}}$ in %	γ_{GENE} in c_s/R_0	ω_{GENE} in c_s/R_0
0.001	0.528	0.676
0.50	0.456	0.730
1.00	0.338	0.777
1.40	0.193	0.779
1.55	0.191	3.107
1.60	0.306	3.026
1.75	0.607	2.824
1.80	0.696	2.771
1.90	0.854	2.678
2.00	0.989	2.597
2.25	1.260	2.434
2.50	1.467	2.302

Between $\beta_{\text{ref}} = 1.5\%$ and 1.55% , the most unstable mode changes character and exhibits much larger frequencies though still propagating in the ion diamagnetic drift direction, thus revealing itself as a kinetic ballooning mode (KBM) or Alfvénic ITG. All of the participating global codes—here, EUTERPE, GENE, GKW, and ORB5—agree well on this qualitative behavior. Quantitatively, excellent agreement is found between the two Eulerian codes GENE and GKW, good agreement with the PIC code ORB5 and reasonable agreement with the other PIC code EUTERPE. The latter is most likely linked to insufficient resolution—corresponding tests are still outstanding due to computational allocation restrictions. It should be noted that due to the reduced linear drive, the global results do not only exhibit smaller growth rates compared to the flux-tube results maximized over the same radial range and ballooning angle but also a different threshold for the KBM branch. This again emphasizes the importance of global electromagnetic simulations for applications to experiments in this parameter regime.

2. Spectral features and mode structures at nominal β

Similar to Sec. IV B, the spectral properties of the low- to intermediate- k modes are studied here, however, in the presence of electromagnetic fluctuations at nominal β ($\sim 1\%$). As shown in Fig. 10 and Table VI, adding A_{\parallel} does not change the overall picture qualitatively. An ITG mode is still present at low- k , whereas a TEM or TEM/ETG-hybrid mode takes over as the most unstable mode between $n_0 = 40$ and 50 . However, quantitatively, the ITG mode is stabilized by up to 30% in wide k range while the impact on the electron diamagnetic drift direction mode is rather negligible. The agreement between the two Eulerian codes GKW and GENE is again very good both in the ion and electron diamagnetic drift frequency branches. Furthermore, ITG mode growth rates and frequencies from the PIC code ORB5 match quite well, although the growth rates are slightly higher—consistently with the results in Fig. 9. The similarities between both numerical approaches can also be confirmed in mode structure comparison at $n_0 = 25$. As can be observed in Figs. 11 and 12, GENE and

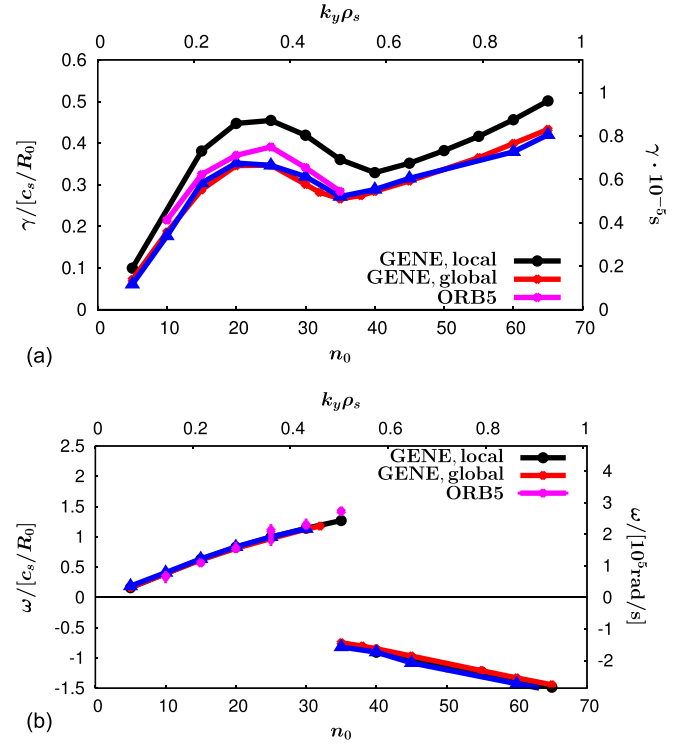


FIG. 10. Linear (a) growth rate and (b) real frequency spectra from ORB5, GKW and GENE for the nominal β case. The local GENE (flux tube) results with linear growth rates maximized over the radius and ballooning angle are plotted for reference, as well.

ORB5 agree well in cross sections and profile plots of the electrostatic potential ϕ and the parallel component of the vector potential A_{\parallel} . Particularly, the anti-ballooning character of the latter is found and confirmed by both codes. However, as in the electrostatic case (Fig. 7), the mode rational surface signatures are not as pronounced with the employed ORB5 field solver as in GENE. This may also explain why the electrostatic potential is found at higher amplitudes at the high field side in GENE. Finally, cross sections of the electrostatic potential and parallel vector field components from GENE at $n_0 = 50$ are shown for reference in Fig. 13. They demonstrate the much more localized eddy structures and much more pronounced

TABLE VI. Data points from global GENE simulations as presented in Fig. 10 for the nominal β case. Growth rates and frequencies (γ, ω) are normalized to $c_s/R_0 = 191.7$ kHz.

n_0	$k_y \rho_s$	γ_{GENE}	ω_{GENE}
5	0.078	0.072	0.163
10	0.157	0.186	0.393
15	0.235	0.288	0.617
20	0.313	0.346	0.809
25	0.391	0.347	0.971
30	0.470	0.301	1.126
35	0.548	0.266	-0.749
40	0.626	0.284	-0.848
45	0.704	0.309	-0.969
55	0.861	0.365	-1.210
60	0.939	0.399	-1.330
65	1.017	0.433	-1.443

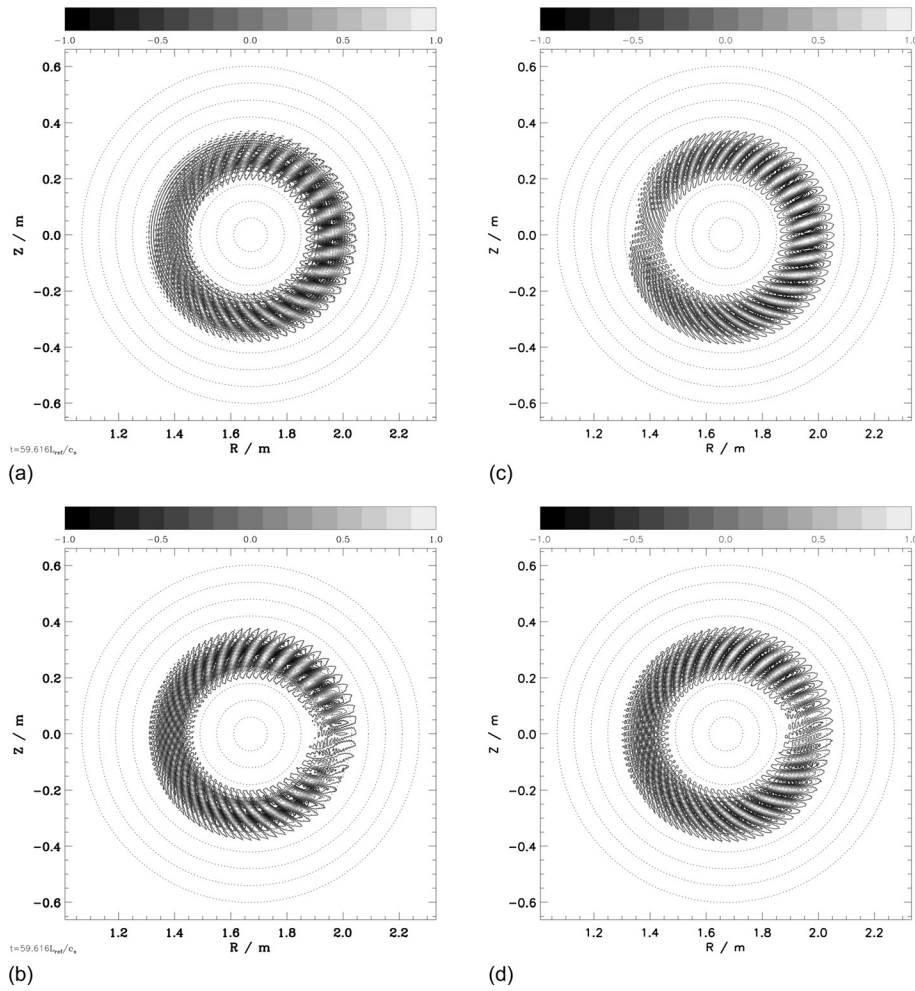


FIG. 11. Mode structure of the rescaled electrostatic potential (left) and parallel vector potential (right) in the (R,Z) plane for the nominal β , two-species case at $n_0 = 25$ from (a), (b) GENE, and (c), (d) ORB5.

fine-scale structures compared to the $n_0 = 25$ results. The radial resolution requirements are hence again found to be quite challenging—up to 30 to 50 radial grid points per ion gyro-radius need to be considered. Studying the relevance of these

restrictions in nonlinear regimes—similarly to corresponding flux-tube investigations²⁹—will be of prime importance in order to assess the computational effort of numerically converged turbulence simulations.

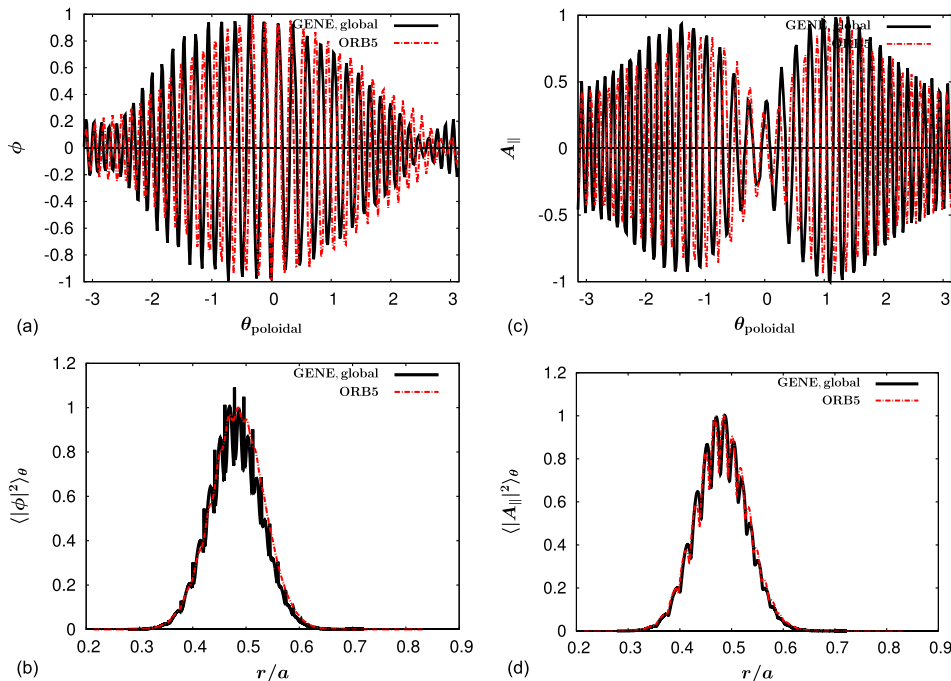


FIG. 12. Direct comparison of the last snapshots of the electrostatic potential (upper row) and A_{\parallel} (lower row) at $n=25$ from GENE (black, solid) and ORB5 (red, dashed) (a), (c) as a function of the poloidal angle at $r/a = 0.5$ (phase adjusted to the dominant poloidal mode number m) and (b), (d) as radial profile of the poloidally averaged squared fluctuations.

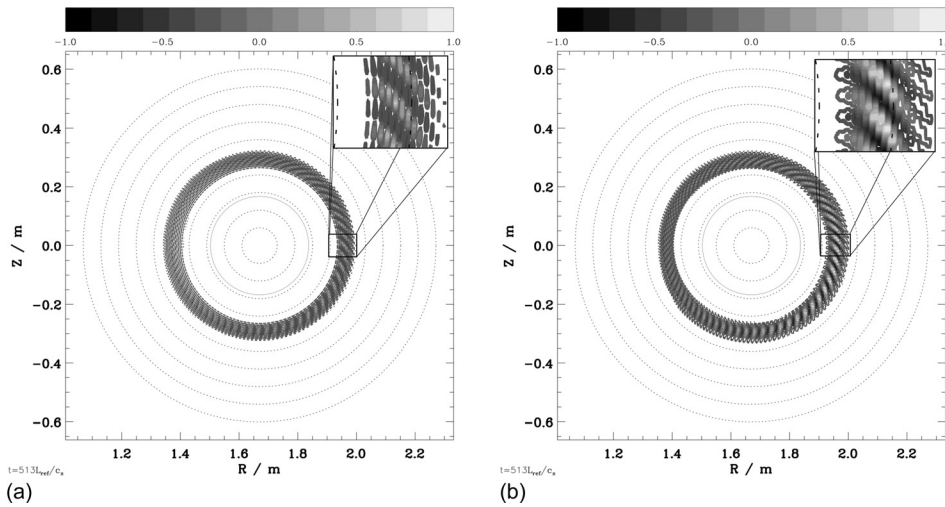


FIG. 13. Mode structure of the rescaled electrostatic potential (left) and parallel vector potential (right) in the (R,Z) plane for the nominal β , 2 species case at $n_0 = 50$ from GENE including zooms into the low field side cross section.

V. CONCLUSIONS

At present, only very few code comparisons—if at all—exist that consider global gyrokinetic electromagnetic finite- n micro-instabilities with entirely different numerical approaches. Obviously, successful benchmarks would greatly improve the confidence regarding a correct implementation and hence contribute along the verification of the codes. As a consequence, a hierarchical test case has been defined in this paper that shall enable and facilitate such comparisons. Starting with the well-studied global ITG mode with adiabatic electrons, more physics has been added progressively until finally mode structures and spectral features of fully electromagnetic modes with kinetic electrons have been addressed. Here, results from a dedicated EUROfusion project involving up to five codes representing three different basic numerical approaches—Eulerian, Lagrangian, and semi-Lagrangian—have been included. Although studies of the linear dynamics are challenging for some of the numerical implementations, a good agreement could be found in the low- k range. At larger wave numbers, deviations have been observed which, however, could clearly be related to certain approximations in the gyro averages and field solvers. A general finding was that fairly high radial resolution up to $\sim 1/20$ of an ion-gyroradius had to be employed when switching to fully gyrokinetically treated electrons. This increase—here found mostly at the larger wave numbers—can at least in parts be related to physical fine-scale structures like mode-rational surfaces. As a result, numerically converged nonlinear global electromagnetic turbulence simulations may be much more challenging and computationally expensive than previously assumed. Of course, linear findings may not simply translate to nonlinear turbulence simulations. However, corresponding evidence has already been found in local, flux-tube simulations.²⁹ An obvious extension of this work would hence be dedicated nonlinear simulations. While relaxation problems may be used for initial comparisons, gradient-driven simulations with carefully defined heat and particle sources and sinks will be prime choice. Such studies are less expensive than flux-driven

simulations, but would allow for sufficient statistics in determining the various turbulence observables.

ACKNOWLEDGMENTS

The authors acknowledge valuable discussions with Julien Dominski, Gabriele Merlo and the participants of the EUROfusion enabling research project ER15-IPP01 on “Verification and development of new algorithms for gyrokinetic codes.” This work has been carried out within the framework of the EUROfusion Consortium and has received funding from the Euratom research and training Programme No. 2014-2018 under Grant Agreement No 633053. The views and opinions expressed herein do not necessarily reflect those of the European Commission. The simulations presented in this work were carried out using the HELIOS supercomputer system at Computational Simulation Centre of International Fusion Energy Research Centre (IFERC-CSC), Aomori, Japan, and at the Max Planck Computing and Data Facility (MPCDF, formerly known as RZG), Garching, Germany.

APPENDIX A: THE MAGNETIC GEOMETRY

The magnetic geometry employed in this benchmark is described by an analytical axisymmetric ad hoc equilibrium model with circular concentric flux surfaces. It is similar to the popular $s - \alpha$ equilibrium with vanishing Shafranov shift ($\alpha = 0$) but more consistent in the large aspect ratio approximation.²⁵ The flux surfaces are parametrized by the minor radius r and their poloidal cross sections are given by $R = R_0(1 + \epsilon \cos \theta)$ and $Z = Z_0 + r \sin \theta$ where θ is the poloidal angle (in counter-clockwise direction), $\epsilon = r/R_0$ the inverse aspect ratio of the flux surface and R and Z denote the horizontal and vertical coordinates. The flux surfaces are centered at the elevation Z_0 which is neglected for simplicity in the following and at the major radius R_0 . The poloidal coordinates are complemented by the toroidal angle ϕ which runs clockwise in a top view such that the full set is (r, θ, ϕ) . The basic assumptions in this model are now a toroidal magnetic field component $B_\phi = B_0 R_0/R$ and a poloidal flux

function Ψ which is defined via its radial derivative $d\Psi/dr = rB_0/\bar{q}(r)$. Here, $B_0 = B_{\text{ref}}$ denotes the magnetic field at the magnetic axis while $\bar{q}(r) = q(r)\sqrt{1-\epsilon^2}$ is just an abbreviation for the modified safety factor profile. With these relations, the magnetic field can be represented by

$$\mathbf{B} = \nabla\phi \times \nabla\Psi + B_\phi \mathbf{e}_\phi = R_0 B_0 / R [\epsilon/\bar{q} \mathbf{e}_\theta + \mathbf{e}_\phi]. \quad (\text{A1})$$

For codes employing field-aligned coordinates, the straight-field-line angle χ is given as follows:

$$\chi = \frac{1}{q} \int_0^\theta \frac{\mathbf{B} \cdot \nabla\phi}{\mathbf{B} \cdot \nabla\theta'} d\theta' = 2\arctan \left[\sqrt{\frac{1-\epsilon}{1+\epsilon}} \tan\left(\frac{\theta}{2}\right) \right]. \quad (\text{A2})$$

¹A. J. Brizard and T. S. Hahm, *Rev. Mod. Phys.* **79**(2), 421 (2007).

²J. A. Krommes, *Annu. Rev. Fluid Mech.* **44**, 175–201 (2012).

³X. Garbet, Y. Idomura, L. Villard, and T. H. Watanabe, *Nucl. Fusion* **50**, 043002 (2010).

⁴C. Bourdelle, W. Dorland, X. Garbet, G. W. Hammett, M. Kotschenreuther, G. Rewoldt, and E. J. Synakowski, *Phys. Plasmas* **10**(7), 2881 (2003).

⁵M. J. Pueschel, M. Kammerer, and F. Jenko, *Phys. Plasmas* **15**(10), 102310 (2008).

⁶E. A. Belli and J. Candy, *Phys. Plasmas* **17**(11), 112314 (2010).

⁷J. A. Baumgaertel, G. W. Hammett, D. R. Mikkelsen, M. Nunami, and P. Xanthopoulos, *Phys. Plasmas* **19**(12), 122306 (2012).

⁸A. Könies, S. Briguglio, N. Gorelenkov, T. Fehér, M. Isaev, P. Lauber, A. Mishchenko, D. Spong, Y. Todo, W. Cooper, R. Hatzky, R. Kleiber, M. Borchardt, G. Vlad, and ITPA EP TG, see http://www-naweb.iaea.org/napc/physics/FEC/FEC2012/papers/437_ITRP134.pdf for 24th IAEA International Conference on Fusion Energy, 2012.

⁹G. L. Falchetto, B. D. Scott, P. Angelino, A. Bottino, T. Dannert, V. Grandgirard, S. Janhunen, F. Jenko, S. Jolliet, A. Kendl, B. F. McMillan, V. Naulin, A. H. Nielsen, M. Ottaviani, A. G. Peeters, M. J. Pueschel, D. Reiser, T. T. Ribeiro, and M. Romanelli, *Plasma Phys. Controlled Fusion* **50**(12), 124015 (2008).

¹⁰J. Candy, R. E. Waltz, and W. Dorland, *Phys. Plasmas* **11**, L25–L28 (2004).

¹¹B. F. McMillan, X. Lapillonne, S. Brunner, L. Villard, S. Jolliet, A. Bottino, T. Görler, and F. Jenko, *Phys. Rev. Lett.* **105**(15), 155001 (2010).

¹²X. Lapillonne, B. F. McMillan, T. Görler, S. Brunner, T. Dannert, F. Jenko, F. Merz, and L. Villard, *Phys. Plasmas* **17**, 112321 (2010).

¹³A. M. Dimits, G. Bateman, M. A. Beer, B. I. Cohen, W. Dorland, G. W. Hammett, C. Kim, J. E. Kinsey, M. Kotschenreuther, A. H. Kritiz, L. L. Lao, J. Mandrekas, W. M. Nevins, S. E. Parker, A. J. Redd, D. E. Shumaker, R. Sydora, and J. Weiland, *Phys. Plasmas* **7**, 969–983 (2000).

¹⁴C. M. Greenfield, J. C. DeBoo, T. H. Osborne, F. W. Perkins, M. N. Rosenbluth, and D. Boucher, *Nucl. Fusion* **37**, 1215–1228 (1997).

¹⁵F. Jenko, W. Dorland, M. Kotschenreuther, and B. N. Rogers, *Phys. Plasmas* **7**, 1904–1910 (2000).

¹⁶T. Görler, X. Lapillonne, S. Brunner, T. Dannert, F. Jenko, F. Merz, and D. Told, *J. Comput. Phys.* **230**, 7053 (2011).

¹⁷A. G. Peeters, Y. Camenen, F. J. Casson, W. A. Hornsby, A. P. Snodin, D. Srintzi, and G. Szepesi, *Comput. Phys. Commun.* **180**, 2650–2672 (2009).

¹⁸R. Buchholz, Y. Camenen, F. J. Casson, S. R. Grosshauser, W. A. Hornsby, P. Migliano, and A. G. Peeters, *Phys. Plasmas* **21**, 062304 (2014).

¹⁹S. Jolliet, A. Bottino, P. Angelino, R. Hatzky, T. Tran, B. McMillan, O. Sauter, K. Appert, Y. Idomura, and L. Villard, *Comput. Phys. Commun.* **177**, 409–425 (2007).

²⁰A. Bottino, T. Vernay, B. Scott, S. Brunner, R. Hatzky, S. Jolliet, B. F. McMillan, T. M. Tran, and L. Villard, *Plasma Phys. Controlled Fusion* **53**, 124027 (2011).

²¹N. Tronko, A. Bottino, and E. Sonnendrücker, e-print [arXiv:1604.03538](https://arxiv.org/abs/1604.03538).

²²V. Kornilov, R. Kleiber, R. Hatzky, L. Villard, and G. Jost, *Phys. Plasmas* **11**, 3196–3202 (2004).

²³V. Grandgirard, M. Brunetti, P. Bertrand, N. Besse, X. Garbet, P. Ghendrih, G. Manfredi, Y. Sarazin, O. Sauter, E. Sonnendrücker, J. Vaclavik, and L. Villard, *J. Comput. Phys.* **217**, 395–423 (2006).

²⁴V. Grandgirard, J. Abiteboul, J. Bigot, T. Cartier-Michaud, N. Crouseilles, G. Dif-Pradalier, Ch. Ehrlacher, D. Esteve, X. Garbet, Ph. Ghendrih, G. Latu, M. Mehrenberger, C. Narscini, Ch. Passeron, F. Rozar, Y. Sarazin, E. Sonnendrücker, A. Strugarek, and D. Zarzoso, “A 5d gyrokinetic full-f global semi-lagrangian code for flux-driven ion turbulence simulations,” *Comput. Phys. Commun.* (in press).

²⁵X. Lapillonne, S. Brunner, T. Dannert, S. Jolliet, A. Marinoni, L. Villard, T. Görler, F. Jenko, and F. Merz, *Phys. Plasmas* **16**, 032308 (2009).

²⁶R. L. Miller, M. S. Chu, J. M. Greene, Y. R. Lin-Liu, and R. E. Waltz, *Phys. Plasmas* **5**, 973–978 (1998).

²⁷A. Bottino and E. Sonnendrücker, *J. Plasma Phys.* **81**, 435810501 (2015).

²⁸J. Dominski, B. F. McMillan, S. Brunner, G. Merlo, T. M. Tran, and L. Villard, “An arbitrary wavelength solver for global gyrokinetic simulations. Application to the study of fine radial structures on microturbulence due to nonadiabatic passing electron dynamics” (unpublished).

²⁹J. Dominski, S. Brunner, T. Görler, F. Jenko, D. Told, and L. Villard, *Phys. Plasmas* **22**, 062303 (2015).